PHYSICAL REVIEW A VOLUME 26, NUMBER 6 DECEMBER 1982

Nonadiabatic theory of collision-broadened atomic line profiles

Paul S. Julienne
Molecular Spectroscopy Division, National Bureau of Standards, Washington, D.C. 20234
(Received 22 April 1982)

The close-coupled theory of atomic scattering in a radiation field can be used to calculate nonadiabatic effects on collision-broadened atomic line profiles. When the strength of the radiation field is not too large, reduced free-free dipole matrix elements, which are independent of the field strength and are analogous to the free-free Franck-Condon factors of line profile theory, can be defined in terms of the S-matrix elements for light-induced atomic scattering. The profile can then be calculated even when the molecular states are mixed by off-diagonal terms in the molecular Hamiltonian due to the breakdown of the Born-Oppenheimer approximation. Numerical close-coupled scattering calculations are used to calculate the profile for the asymptotically forbidden, collision-induced radiative transition $O\,^1S + Ar \rightarrow O\,^1D + Ar + h\nu$. The profile was calculated in two ways: (1) with the use of the normal Born-Oppenheimer approximation for the final states and (2) with the use of the new technique to treat the nonadiabatic mixing among the $^1\Sigma$, $^1\Pi$, and $^1\Delta$ final states. The Coriolis interaction mixes the Hund's case-(a) Λ states asymptotically to give Hund's case-(e) states. The central and red-wing parts of the profile which originate primarily from large internuclear separations are strongly affected by this mixing. The calculated profile which takes this mixing into account agrees well with the experimental profile but differs significantly from the Born-Oppenheimer profile. The differences are explained in terms of intensity borrowing and Hund's case-(e) selection rules.

I. INTRODUCTION

The phenomenon of atomic scattering in the presence of a radiation field has been the subject of much interest recently, both experimentally and theoretically. Several experiments have given ample demonstration of "radiative collisions," or laser-switched collisions,[1-6] as well as providing new studies in the more traditional area of "optical collisions," or wing line broadening.[7,8] Theoretical developments have included both full quantum-mechanical close-coupling formulations[9-12] and various semiclassical approaches.[13-20] Since the atomic scattering cross section departs from linearity in the light intensity only for very intense lasers, typically requiring power fluxes $> 10^8$ W cm^{-2}, the bulk of light-induced atomic scattering phenomena can be treated quite satisfactorily by treating the interaction between the light and the atoms perturbatively.[12,21] In this case, the theory of light-induced atomic scattering simply becomes a generalization of the highly developed traditional field of collision-broadened atomic line profiles.[17,22] In fact, we propose to show in this paper how the quantum close-coupled treatment of light-induced atomic scattering can be used to calculate nonadiabatic effects on collision-broadened profiles.

Let us restrict our attention either to the case of asymptotically forbidden transitions or to the wings of asymptotically allowed transitions. Thus, we consider only that part of the profile that can be adequately described in terms of single binary collisions, represented by the equation

$$A + R + nh\nu \rightarrow A' + R' + (n \pm 1)h\nu \ , \tag{1}$$

when an atom A collides with a perturber R in the presence of n photons of energy $h\nu$ (assuming a single mode laser) and undergoes a transition to state A' with the corresponding absorption or stimulated emission of a single photon. The collision partner R may or may not change states. Energy conservation during a particular collision requires

$$E = E_i + \epsilon_i + nh\nu = E_f + \epsilon_f + (n \pm 1)h\nu \ , \tag{2}$$

where E_i and E_f are the total internal energies of the initial and final separated atom states and ϵ_i and ϵ_f are the center-of-mass initial and final kinetic energies. This may alternatively be expressed as

$$h\nu = h\nu_0 + \Delta \ , \tag{3}$$

where $h\nu_0 = |E_f - E_i|$ is the asymptotic transition

energy and $\Delta=\pm(\epsilon_i-\epsilon_f)$ is the shift from the asymptotic energy.

The total rate of change of photon or atomic densities, denoted by ρ and ρ_A, respectively, is[21]

$$\pm\frac{\partial\rho}{\partial t}=-\frac{\partial\rho_A}{\partial t}=K(v)\rho_A\rho_R \ , \tag{4}$$

where the two-body rate coefficient

$$K(v)=\langle\sigma(\epsilon_i)v_i\rangle \tag{5}$$

represents the σv average of the cross section for (1) over the distribution of initial velocities v_i, normally taken to be thermal. The photon absorption or stimulated emission coefficient per unit length, defined by

$$k(v)=\frac{1}{\phi}\frac{\partial\phi}{\partial z} \ , \tag{6}$$

where $\phi=c\rho$ is the photon flux (photons $\mathrm{cm}^{-2}\mathrm{sec}^{-1}$), is found from (4) by replacing $\partial/\partial t$ by $c\partial/\partial z$:

$$k(v)=\frac{K(v)}{\phi}\rho_A\rho_R \ . \tag{7}$$

For the case of spontaneous emission, the total rate of emission into frequency interval dv, summed over all possible directions and polarizations of the emitted photon,

$$k_{se}(v)\rho_A\rho_R dv \ , \tag{8}$$

is related to the stimulated emission rate through[21]

$$k_{se}(v)=\frac{8\pi}{\lambda^2}\frac{K(v)}{\phi} \ , \tag{9}$$

where $\lambda=c/v$ is the wavelength. Thus, a knowledge of the profile function $K(v)/\phi$ permits us to characterize both the strength and frequency dependence of absorption or spontaneous and stimulated emission.

The object of line profile theory is to find the function $K(v)/\phi$. This quantity is independent of light intensity ϕ so long as ϕ is not too large, since $K(v)$ is linear in ϕ. In this limit, the profile function depends only on the properties of the molecular states of the diatomic species AR and on the transition dipole moments between them. In traditional line profile theory the quantum-mechanical profile is written in terms of matrix elements of the type $\langle\epsilon_i\,|\,\mu(R)\,|\,\epsilon_f\rangle$, where $|\,\epsilon_i\rangle$ and $|\,\epsilon_f\rangle$ represent energy normalized vibrational continuum states in the initial and final states and $\mu(R)$ represents an R-dependent electronic transition dipole, where R is the internuclear separation. Although fully quantum-mechanical calculations of such matrix elements are straightforward, they are time consuming and tedious, and only a few have been reported.[23–26] Normally, introduction of the semiclassical WKB approximation followed by applications of the stationary-phase and random-phase approximations has been used to justify use of the simple quasistatic expressions for the thermally averaged profile.[26,27] Semiclassical theories utilizing Fourier transforms of the difference potential have also been introduced.[22] These do not make the stationary-phase approximation and thus avoid divergences associated with quasistatic theories.[26]

All of these theories rely on the assumption that the motion in the initial or final state is based on a single molecular potential, that is, they invoke the Born-Oppenheimer approximation. Although this simplifying approximation is normally adequate for describing the far wings of the profile where the motion is often predominately based on isolated electronic potentials, it becomes suspect if the molecular potentials cross or come close to each other. Generally, the possibility of a problem exists in the case of laser-switched collisions when one or both of the asymptotic states is degenerate. The asymptotically energies of the several Λ states originating from the degenerate asymptote split apart as the atoms approach each other and coalesce as the atoms separate. The small Coriolis coupling terms in the Hamiltonian that are proportional to R^{-2} (where R is the internuclear separation) are normally not very significant at short range, but are dominant at long range and mix the Λ states asymptotically.[28] In fact, this mixing is absolutely necessary in order to go between a Hund's case-(a) representation where the molecular Hamiltonian is nearly diagonal in a rotating molecule-fixed frame at small R to a Hund's case-(e) representation in which H is asymptotically diagonal in a space-fixed frame.[28–30] Although this switching of representations can often be described in terms of a quantum-mechanical "sudden" approximation,[28,30] this effect can be nontrivial for laser-switched collisional line profiles due to the long-range nature of the transition moments, which vary as R^{-3} or R^{-4}. Since the molecular states are split as R^{-6} at long range, the R^{-2} Coriolis terms can be dominant at the large internuclear separations which contribute to the central-peak region of the profile. It is this aspect of Born-Oppenheimer breakdown that we will study in this paper. The theory is, of course, also capable of treating other types of Born-Oppenheimer breakdown for short-range-potential crossings.

A scattering-theory formulation of the atomic

collisions in the presence of the radiation field gives a simple and natural alternative way to find the profile function and avoid the difficulties associated with the Born-Oppenheimer approximation. Since both the radiative and internal molecular interactions are treated on an equal footing, the Born-Oppenheimer approximation need never be invoked (other than to provide a convenient expansion basis), and nonadiabatic effects on the profile can be readily treated. The theory gives the cross section required in (5) directly. If the light intensity ϕ is not too large, the distorted-wave approximation can be used for the S-matrix elements. The resulting expression for the profile is identical to the expression of ordinary line profile theory, but with one important difference: The S matrix includes the effect of nonadiabatic couplings among the molecular states. Therefore, the scattering theory can be used to define a generalized reduced free-free vibrational overlap factor which is not dependent on the Born-Oppenheimer approximation but which reduces to the conventional factor when the Born-Oppenheimer approximation applies.

The present paper summarized the theory of light-induced atomic scattering, which has been described in detail by Mies,[12] and illustrates its application by calculating the profile for the collision-induced emission

$$\mathrm{O}\,^1S+\mathrm{Ar}\rightarrow\mathrm{O}\,^1D+\mathrm{Ar}+h\nu\ . \tag{10}$$

The $\mathrm{O}\,^1S\rightarrow\mathrm{O}\,^1D$ transition is forbidden asymptotically (as $R\rightarrow\infty$), and the long-range induced transition dipole moment varies as R^{-4}. The reaction serves as a prototype of a laser-switched collision with an asymptotically vanishing transition moment. The emission profile has previously been calculated, both quantum mechanically[25] and with the quasistatic approximation,[31] using the Born-Oppenheimer approximation with *ab initio* potentials and transition moments. Experimental measurements of the total emission rate[32–35] and profile[36,37] have also been made. The agreement between the calculation and measurement is excellent for the total emission coefficients (i.e., integrated over all $h\nu$) and the quasistatic blue-wing profile.[31] However, the calculations completely fail to reproduce the peak and red-wing region of the profile. We have recalculated the profile using the closed-coupled scattering approach and now find good agreement with the whole experimental profile. There are intrinsic close-coupling effects associated with the switching between a short-range molecule-fixed and long-range space-fixed representation of the wave function. These effects lead to a significant redistribution of intensity in the central and red-wing regions of the profile. An interpretation of this redistribution is facilitated by introducing the adiabatic electronic-rotational states described by Mies.[38]

Section II of the paper summarizes the close-coupling scattering theory and relates it to the profile function. Section III describes the molecular Hamiltonian including the radiation field. Section IV describes the results of the calculation and summarizes the conclusions.

II. CLOSE-COUPLING THEORY

The quantum close-coupling theory of atomic scattering in radiation fields has been described elsewhere.[12] We will summarize here those aspects of the theory which are pertinent to the calculation of the line profile function. The object is to determine the scattering probability for the atomic collision described by Eq. (1). Let us assume that the initial asymptotic atomic states of $A+R$ are nondegenerate. This assumption simplifies the notation and discussion, corresponds to the actual system we will study, and is not restrictive in that it may be removed in a straightforward way by introducing an additional summation over initial states.

The theory of light-induced scattering does not treat the interactions of the atoms with light merely as time-dependent perturbations which induce transitions between molecular states, but determines the states of the matter-radiation system described by the Hamiltonian

$$H=H^{AR}+H^{\mathrm{rad}}+V^{\mathrm{rad}}\ . \tag{11}$$

H^{AR} is the Hamiltonian of the isolated molecule AR, H^{rad} is the Hamiltonian of the isolated radiation field, and V^{rad} gives the coupling between the radiation and the molecule. The total wave function is expanded in a product basis set of the type

$$\{\,|\,g\,\rangle\}=\{\,|\,JMpr\,\rangle\otimes|\,n_\lambda\,\rangle\}\ . \tag{12}$$

Here $|\,JMpr\,\rangle$ is an eigenstate of the electronic-rotational part of H^{AR} and $|\,n_\lambda\,\rangle$ is an eigenstate of H^{rad}. The quantum numbers J, M, and p, respectively, represent total molecular angular momentum, its space-fixed projection along an arbitrary axis, and parity ±1 with respect to inversion of *all* coordinates. The corresponding operators commute with H^{AB} and each other, and these quantum numbers are rigorous (conserved) for an isolated mole-

cule. The quantum number r represents all the other approximate quantum numbers needed to characterize a molecular state. The radiation eigenstate for mode λ of the radiation field represents n photons of frequency $h\nu$ and polarization vector $\hat{e}_0$ (linear polarization is assumed here). The field angular momentum is not quantized here and does not concern us. Since we will be summing over molecular angular momentum projection states, the choice of the arbitrary quantization axis may be taken to be along $\hat{e}_0$ for convenience. In this case, the selection rule that M is conserved applies (see below and Ref. 12).

The total molecule-field wave function at total energy E, given by (2), can be expanded in the basis (12) as follows:

$$\Psi_j^{JM}(E)=|i\rangle F_{ij}(E,R)/R + \sum_f |f\rangle F_{fj}(E,R)/R \ , \tag{13}$$

where R is the internuclear separation. The quantum numbers g in the basis $|g\rangle$ contain all of the quantum numbers needed to describe the internal states and relative angular momentum of the asymptotic fragments and therefore label the scattering channels. A partial-wave expansion has been assumed in which the initial state has total angular momentum J and projection M. The state $|i\rangle$ is thus characterized by the atoms A and R in their initial nondegenerate states, the molecular quantum numbers JMp, and n photons of polarization $\hat{e}_0$. The final state $|f\rangle$ is characterized by the A' and R' atoms in one of their degenerate states distinguished by the appropriate channel quantum number, the molecular quantum numbers $J_f M_f p_f$, and $n\pm1$ photons of polarization $\hat{e}_0$. Radiative selection rules impose the restriction $J_f=J, J\pm1$, $M_f=M$, $p_f=-p$ (see below). The label J is applied to the total wave function, since specification of the initial J uniquely determines the possible final J's through the radiative selection rules. The quantum numbers j on ψ indicate an incoming wave in channel j, which could be either i or f.

The task of scattering theory is to determine the amplitudes $F(E,R)$ in (13) and extract the S-matrix elements from them. Substitution of (13) into the Schrödinger equation leads to the coupled equations for the amplitudes:

$$\left[\frac{\hbar^2}{2\mu}\frac{d^2}{dR^2}+E-V_i-n\hbar\nu\right]F_{ii}=\sum_f V_{if}^{\rm rad}F_{fi} \ , \tag{14a}$$

$$\left[\frac{\hbar^2}{2\mu}\frac{d^2}{dR^2}+E-V_f-(n\pm1)h\nu\right]F_{ff} = \sum_{f'} H_{ff'}^{AB}F_{f'f}+V_{fi}^{\rm rad}F_{if} \ , \tag{14b}$$

where μ is the reduced mass of the colliding pair of atoms. The potentials $V_j(R)$ represent the sum of the electronic and rotational energies and are discussed in more detail in Sec. III. The difference of one photon between initial and final states ensures that the upper and lower effective potentials $V_j+n_jh\nu$ cross at the stationary phase points of the semiclassical theory. The $V^{\rm rad}$ matrix elements give the radiative couplings, and the H^{AB} matrix elements include all the couplings between the degenerate set of final states that lead to breakdown of the Born-Oppenheimer approximation.

The S matrix is determined from the amplitudes F by imposing the proper asymptotic boundary conditions. Assuming that all off-diagonal elements of H vanish asymptotically, we require[12]

$$F_{jj'}=-i\left[\frac{\mu}{2\pi\hbar^2k_{j'}}\right]^{1/2}\left[\delta_{jj'}\exp[-i(k_{j'}R-\tfrac{1}{2}\pi l_{j'})]-S_{jj'}\left[\frac{k_{j'}}{k_j}\right]^{1/2}\exp[i(k_jR-\tfrac{1}{2}\pi l_j)]\right] , \tag{15}$$

where $k_j=(2\mu\epsilon_j/\hbar)^{1/2}$ is the asymptotic wave vector in channel j. The S-matrix elements can be used to predict the cross section for any scattering experiment corresponding to (1), for example, the differential cross section for producing the final-state atoms in a particular one of their degenerate quantum states. However, we are concerned here only with the *total* probability of light-induced scattering from the initial to the final set of states for a homogeneous ensemble of atoms. A future paper is planned which treats the problem of state-to-state profiles. For the present, we require only

$$P^J(\epsilon,\Delta)=\frac{1}{2J+1}\sum_f\sum_{M=-J}^{J}\left|S_{fi}^{JM}(\epsilon,\Delta)\right|^2 . \tag{16}$$

Equation (16) gives the probability of a radiative transition from the initial state to the final states for photons with energy shift Δ and for a particular initial-state kinetic energy ϵ and angular momentum J. The probability is averaged over the $2J+1$ space-fixed projections M. The probability (16) is the quantum-mechanical expression which corre-

sponds to the semiclassical expression used by Gallagher and Holstein.[22]

The cross section for light-induced scattering is

$$\sigma(\epsilon,\Delta)=\frac{\pi}{k_i^2}\sum_{J=0}^{\infty}(2J+1)P^J(\epsilon,\Delta)\ . \tag{17}$$

The rate coefficient of Eq. (5) for a Maxwell-Boltzmann velocity distribution at temperature T is[39]

$$K(\Delta,T)=\frac{1}{Q_T}\int_0^{\infty}\frac{1}{h}\sum_J(2J+1)P^J(\epsilon,\Delta)\times e^{-\epsilon/k_BT}d\epsilon\ , \tag{18}$$

where

$$Q_T=(2\pi\mu k_BT/h^2)^{3/2}$$

is the translational partition function and k_B is the Boltzmann constant. Note that the frequency argument is now written in terms of Δ instead of ν.

Although all that is needed to calculate the profile function in (18) is a straightforward scattering calculation, considerable insight is gained if we make use of the intrinsic smallness of the radiative coupling $V^{\rm rad}$. As long as the intensity of the radiation field is less than some threshold value (typically $10^8\,{\rm W\,cm^{-2}}$, although this can vary by several orders of magnitude in either direction depending on the particular problem), the scattering probability $P^J(\epsilon,\Delta)$ is much less than unity, and the standard distorted-wave approximation with respect to the radiative coupling can be used for the S-matrix elements[12]

$$S_{fi}^{JM}(\epsilon,\Delta)=-2\pi i\langle{}^*\epsilon_fJ_f\,|\,V_n^{\rm rad}\,|\,\epsilon J\rangle\ , \tag{19}$$

where $|\,\epsilon J\rangle$ and $|\,{}^*\epsilon_fJ_f\rangle$ are the energy normalized initial and final radiatively uncoupled solutions to the equations (14) in which the $V^{\rm rad}$ matrix elements have been set equal to zero. The radiative part of the wave function has been eliminated by taking the matrix element of $V^{\rm rad}$ over the radiative coordinates, assuming $n\gg1$. For our geometry this is found to be[12]

$$V_n^{\rm rad}=\langle n\pm1\,|\,V^{\rm rad}\,|\,n\rangle=\left[\frac{2\pi h\phi}{\lambda}\right]^{1/2}\mu_0^{\rm sp}\ , \tag{20}$$

where $\mu_0^{\rm sp}$ is the projection of the molecular dipole operator on the space-fixed z axis defined by $\hat{e}_0$.

The molecular wave functions in (19) are solutions of the coupled equations (14) for the molecule Hamiltonian H^{AB} in the absence of radiative coupling

$$|\,\epsilon J\rangle=|\,JM_pr_i\rangle F_{ii}^0(\epsilon_i,R)/R\ , \tag{21a}$$

$$|\,{}^*\epsilon_fJ_f\rangle=\sum_{f'}|\,JMp_fr_f\rangle F_{f'f}^{0*}(\epsilon_f,R)/R\ . \tag{21b}$$

The asterisk in (21b) implies an outgoing scattering wave for the final state. Although the phase information in the S-matrix is required if we want to predict the state-to-state cross sections giving the distribution of final states, calculating the scattering probability in (16) requires only the squared magnitudes of the S-matrix elements. For this purpose we can also choose to use in (19) real wave functions with standing-wave boundary conditions.

Since the molecular dipole operator $\underline{\mu}^{\rm sp}$ is a spherical tensor of rank 1 and since the molecular wave functions in (19) are eigenstates of total molecular angular momentum, the Wigner-Eckart theorem[40] can be used to give the dependence of the matrix element in (19) on M. Thus, we define a reduced dipole matrix element by

$$\langle{}^*\epsilon_fJ_f\,|\,\mu_0^{\rm sp}\,|\,\epsilon J\rangle=\langle{}^*\epsilon J\,|\,\mu_0^{\rm sp}\,|\,\epsilon_fJ_f\rangle\equiv(J_f1J\,|\,M0M)(\epsilon J||\mu||\epsilon_fJ_f)\ . \tag{22}$$

We could just as easily have used the factor $(J\,1J_f\,|\,M\,0M)$. The definition in (22) was made for convenience in carrying out the M average

$$\frac{1}{2J+1}\sum_{M=-J}^{J}|\,\langle{}^*\epsilon_fJ_f\,|\,\mu_0^{\rm sp}\,|\,\epsilon J\rangle\,|^2=\tfrac{1}{3}\,|\,(\epsilon J||\mu||\epsilon_fJ_f)\,|^2\ . \tag{23}$$

Using (19), (20), and (23) in (16) gives from (18) the weak-field line profile function

$$\frac{K(\Delta,T)}{\phi}=\frac{8\pi^3}{3\lambda}\frac{1}{Q_T}\int_0^{\infty}D_\epsilon(\Delta)e^{-\epsilon/k_BT}d\epsilon\ , \tag{24}$$

where

$$D_\epsilon(\Delta)=\sum_{J=0}^{\infty}(2J+1)\sum_f|\,(\epsilon J||\mu||\epsilon_fJ_f)\,|^2 \tag{25}$$

is the degeneracy-weighed sum over reduced dipole matrix elements.

We see that introduction of the radiative distorted-wave approximation into the close-coupled scattering theory leads to expressions (24) and (25) in terms of free-free dipole overlap matrix elements similar to those of normal line profile theory but generalized to nonadiabatic wave functions. Thus, one approach to calculating the profile is to explicitly evaluate the integrals in (25) using numerical close-coupled wave functions. However,

this is tedious and unnecessary. The scattering theory permits a much simpler approach, that is, calculate the S matrix required in (16) directly by solving the coupled equations (14) with nonvanishing $V^{\rm rad}$ for an arbitrarily chosen small value of the intensity ϕ. Any of the standard close-coupling computer codes can be used for this. A reduced free-free dipole overlap matrix element equivalent to that in (22) can be *defined* in terms of the S matrix instead of in terms of an overlap integral

$$(\epsilon J||\mu||\epsilon_f J_f)\equiv\frac{i}{2\pi}\left[\frac{\lambda}{2\pi h\phi}\right]^{1/2}\frac{S_{fi}^{JM}(\epsilon,\Delta)}{(J_f 1J\,|\,M0M)}\ . \tag{26}$$

This will be independent of ϕ if ϕ is not too large. The calculation need be done only for a single (arbitrary) value of M. In fact, we follow the suggestion of DeVries and George[11] of replacing $(J_f 1J\,|\,M0M)$ by its root-mean-square value, $1/\sqrt{3}$, both in (26) and in the $V^{\rm rad}$ matrix elements used in (14). This automatically leads to the proper M average of (23).

III. SCATTERING HAMILTONIAN

A. Electronic-rotational Hamiltonian and basis

The molecular Hamiltonian H^{AR} in (11) is

$$H^{AR}=-\frac{\hbar^2}{2\mu R^2}\frac{\partial}{\partial R}R^2\frac{\partial}{\partial R}+B(\underline{J}-\underline{L}-\underline{S})^2 +H_e(\underline{r},R)+H_\alpha\ , \tag{27}$$

where $B(R)=\hbar^2/2\mu R^2$. The second term gives the rotational kinetic energy BN^2, where $\underline{N}=\underline{J}-\underline{L}-\underline{S}$ is written in terms of the total angular momentum $\underline{J}$, electronic angular momentum $\underline{L}$, and spin angular momentum $\underline{S}$. The third term H_e is the electronic Hamiltonian, where $\underline{r}$ denotes the collection of all electron coordinates. The last term H_α representing the relativistic corrections that give rise to fine structure, will be neglected in this paper, since it introduces nonessential complications and the reaction (10) studied involves only singlet states ($\underline{S}=0$).

We must now find a suitable set of electronic-rotational basis functions, $|JMpr\rangle$ in (12) in order to calculate the matrix elements in the coupled equations (14). For this purpose, we will use the conventional Hund's case-(a) Born-Oppenheimer basis,[41] although this necessarily leads to a nondiagonal Hamiltonian at large R whenever the separated atomic states are degenerate.[38] These symmetric-top wave functions are eigenstates of $\underline{J}^2$, the projection of $\underline{J}$ on a space-fixed axis, and the projection of $\underline{J}$ on the rotating internuclear axis of the molecule, having respective eigenvalues $J(J+1)$, M, and Λ. The case-(a) basis functions with definite parity are explicitly[39]

$$|JM0p_+\rangle=\left[\frac{2J+1}{4\pi}\right]^{1/2}D^{J*}_{M0}\psi^e_0 \tag{28a}$$

for a $\Lambda=0(\Sigma)$ state, and

$$|JM,|\Lambda|,p_\pm\rangle =\left[\frac{2J+1}{4\pi}\right]^{1/2}\frac{1}{\sqrt{2}}(D^{J*}_{M,\Lambda}\psi^e_\Lambda\pm D^{J*}_{M,-\Lambda}\psi^e_{-\Lambda}) \tag{28b}$$

for a $\Lambda\neq0$ state. In the above $D^{J*}(\alpha,\beta,0)$ is the Wigner rotation matrix, where α and β are the Euler angles giving the orientation of the internuclear axis with respect to the space-fixed coordinate system. The electronic wave functions $\psi^e_\Lambda(\underline{r},R)$ are the eigenstates of $H_e(\underline{r},R)$ for a fixed value of R:

$$H_e(\underline{r},R)\psi^e_\Lambda(\underline{r},R)=W_\Lambda(r)\psi^e_\Lambda(\underline{r},R)\ . \tag{29}$$

The eigenvalue $W_\Lambda(R)$ is just the ordinary Born-Oppenheimer potential energy curve. The parity label p_+ refers to the e states with parity $(-1)^J$, whereas p_- labels the f states with parity $-(-1)^J$.

The calculation of the Hund's case-(a) matrix elements is straightforward.[39] The rotational matrix elements can be readily evaluated by using the expansion

$$(\underline{J}-\underline{L})^2=J^2+L^2-J_z^2-L_z^2-J_+L_--J_-L_+\ , \tag{30}$$

where the projections J_z and L_z are on the rotating internuclear axis. In general, the matrix elements of L^2 and $L_\pm$ cannot be evaluated analytically, but must be calculated from the actual wave function ψ^e_Λ. Since our model problem (10) involves only weak van der Waals interactions, it is an excellent approximation to use matrix elements for the pure L states of the atoms, e.g., for $L=2$ in the case of the molecular states from the O ^1D asymptote.

The O ^1S + Ar ^1S asymptote gives rise to a single $^1\Sigma^+$ molecular state of ArO, for which the diagonal electronic-rotational matrix element is

$$V_i(R)=W_{0i}(R)+B(R)J_i(J_i+1)\ , \tag{31}$$

where $W_{0i}(R)$ is the $^1\Sigma^+$ Born-Oppenheimer potential. The parity is p_+. The O ^1D + Ar ^1S asymptote is fivefold degenerate and gives rise to

$^1\Sigma^+$, $^1\Pi$, and $^1\Delta$ molecular states. The 5×5 electronic-rotational Hamiltonian matrix blocks into a 3×3 block of p_+ parity containing contributions from the $^1\Sigma^+$, $^1\Pi$, and $^1\Delta$ states and a 2×2 block of p_- parity containing contributions from only the $^1\Pi$ and $^1\Delta$ states. The diagonal electronic-rotational matrix elements for these final states are

$$V_{\Lambda f}(R)=W_{\Lambda f}(R) +B(R)[J_f(J_f+1)+6-2\Lambda^2] , \quad (32)$$

where $6=L(L+1)$ comes from assuming a pure $L=2$ state independent of R. The $^1\Sigma$ and $^1\Pi$ and the $^1\Pi$ and $^1\Delta$ states are coupled by the $-B(J_+L_-+J_-L_+)$ Coriolis coupling term in the Hamiltonian. The 1×1, 2×2, and 3×3 electronic-rotational Hamiltonian blocks for the initial and final states are shown in Table I.

When the atoms are close together (R in the vicinity of the van der Waals well), the differences between the electronic potentials, $W_{1f}-W_{0f}$ and $W_{2f}-W_{1f}$, are generally large compared to the Coriolis couplings, which are approximately proportional to BJ. In this case the 2×2 and 3×3 sets of coupled equations (14b) which describes the states from $^1D+^1S$ in the absence of radiative coupling (i.e., with $V^{\rm rad}=0$) may be approximated as uncoupled equations by ignoring the off-diagonal terms. This, of course, is just the normal Born-Oppenheimer approximation and is satisfactory for describing the small-amplitude motion of the vibration-rotational bound states in the van der Waals wells. The effect of the off-diagonal Coriolis terms is to introduce perturbations among bound states of different Λ and Λ doubling in the $^1\Pi$ state.

However, a very different situation applies when the atoms are far apart. At large R, the off-diagonal parts of the electronic-rotational Hamiltonian become dominant compared to the diagonal differences, since the former vanish as R^{-2} whereas the latter vanish as R^{-6}. Thus, at sufficiently large R, the Born-Oppenheimer Λ states are strongly mixed by the Coriolis couplings.[28,29] This mixing occurs for distances where

$$2BJ \gtrsim \max(\,|W_{2f}-W_{1f}|\,,\,|W_{1f}-W_{0f}|\,) . \quad (33)$$

For ArO this applies for $R \geq 8a_0$ for the dominant partial waves contributing to the profile.

The physical meaning of this Coriolis coupling is clear. When the atoms are far apart it is not proper to characterize the molecular states by the projection of electronic angular momentum on the molecular axis. The proper quantization of angular momentum is in a space-fixed frame. These Coriolis terms are the terms in the Hamiltonian which effect the switching between rotating molecule-fixed quantization of $\underline{L}$ at small R and space-fixed quantization of large R. This switching is a general phenomena which *always* occurs when one or both of the asymptotic fragments are nondegenerate. The $(a)\leftrightarrow(e)$ switching is an uncoupling phenomenon analogous to the well-known uncou-

TABLE I. Electronic-rotational Hamiltonian matrix elements [$X\equiv J(J+1)$].

State	Matrix
	$^1S+^1S$; $(-1)^J$ parity.
$^1\Sigma^+$	$(W_{0i}+BX_i)$
	$^1D+^1S$; $-(-1)^J$ parity.
$^1\Pi$, $^1\Delta$	$\begin{pmatrix} W_{1f}+B(X_f+4) & -2B\sqrt{X_f-2} \\ -2B\sqrt{X_f-2} & W_{2f}+B(X_f-2) \end{pmatrix}$
	$^1D+^1S$; $(-1)^J$ parity.
$^1\Sigma^+$, $^1\Pi$, $^1\Delta$	$\begin{pmatrix} W_{0f}+B(X_f+6) & -B\sqrt{12X_f} & 0 \\ -B\sqrt{12X_f} & W_{1f}+B(X_f+4) & -2B\sqrt{X_f-2} \\ 0 & -2B\sqrt{X_f-2} & W_{2f}+B(X_f-2) \end{pmatrix}$

pling cases of bound-state spectroscopy,[42] for example, case (a) to case (b) where spin $\underline{S}$ becomes uncoupled from the rotating axis with increasing J, or case (a) to (d) where $\underline{L}$ becomes uncoupled from the rotating axis with increasing principal quantum number of a Rydberg series.

In order to calculate the S matrix from the asymptotic solutions of (14), these must be written in a channel state representation in which H^{AB} is diagonal as $R \rightarrow \infty$. This clearly cannot be done using the Hund's case-(a) representation of Table I. (See Ref. 38.) The proper asymptotic states can be constructed in either of two ways. One way is simply to diagonalize the 2×2 and 3×3 Hamiltonian blocks in Table I and make a unitary transformation of basis. In the present case this is straightforward and can be done analytically. Alternatively, we may make use of the properties of the angular momentum eigenstates and Wigner rotation matrices.[43]

The asymptotic colliding atoms are eigenstates of electronic angular momentum $\underline{L}^2$ and nuclear rotation angular momentum $(\underline{J}-\underline{L})^2$, characterized by the respective quantum numbers L and l and space-fixed projection quantum numbers M_L and m_l. The $|LM_L\rangle$ states are related by the rotation matrix to the $|L\Lambda\rangle$ states having projection of $\underline{L}$ quantized on the rotating molecular axis[41]

$$|LM_L\rangle = \sum_{\Lambda=-L}^{L} D^{L*}_{M_L\Lambda}(\alpha,\beta,0)\psi^e_\Lambda \ . \tag{34}$$

The eigenstates of $|lm_l\rangle$ can also be written

$$|lm_l\rangle = y_{lm_l}(\beta,\alpha) = \left[\frac{2l+1}{4\pi}\right]^{1/2} D^{l*}_{m_l 0}(\alpha,\beta,0) \ . \tag{35}$$

The $|LM_L\rangle, |lm_l\rangle$ states can be coupled to make states of total J and $M = m_l + m_L$. Using (34), (35), and the properties of the rotation matrixes, we find[43]

$$|JMLl\rangle = \sum_{\Lambda=-L}^{L} (-1)^{L+\Lambda}(JLl\,|\,-\Lambda,\Lambda,0) \times \left[\frac{2J+1}{4\pi}\right]^{1/2} D^{J*}_{M\Lambda}\psi^e_\Lambda \ . \tag{36}$$

The states described by (36) correspond to a Hund's case-(e) coupling scheme.[29,30]

Equation (36) shows the relation between the desired channel-state basis and the Hund's case-(a) basis. It is simple to rewrite (36) in terms of the parity eigenstates (28). Table II shows the coefficients of the unitary transformation between the Hund's case-(a) Born-Oppenheimer basis (28) and the Hund's case-(e) channel-state basis with parity:

$$|JMLlp\rangle = \sum_{\Lambda=0}^{L} C^{JLp}_{\Lambda l}\,|JML,|\Lambda|,p\rangle \ . \tag{37}$$

The transformations (37) diagonalize the 2×2 and 3×3 electronic-rotational Hamiltonian blocks

TABLE II. $C^{JLp}_{\Lambda l}$ transformation from case (a) to case (e).

	$-(-1)^J$ parity	
	$^1\Pi$	$^1\Delta$
$l=J-1$	$-\left[\frac{J-1}{2J+1}\right]^{1/2}$	$-\left[\frac{J+2}{2J+1}\right]^{1/2}$
$l=J+1$	$\left[\frac{J+2}{2J+1}\right]^{1/2}$	$-\left[\frac{J-1}{2J+1}\right]^{1/2}$

	$(-1)^J$ parity		
	$^1\Sigma^+$	$^1\Pi$	$^1\Delta$
$l=J-2$	$\left[\frac{3J(J-1)}{2(2J-1)(2J+1)}\right]^{1/2}$	$\left[\frac{2(J-1)(J+1)}{(2J-1)(2J+1)}\right]^{1/2}$	$\left[\frac{(J+1)(J+2)}{2(2J-1)(2J+1)}\right]^{1/2}$
$l=J$	$-\left[\frac{J(J+1)}{(2J-1)(2J+3)}\right]^{1/2}$	$-\left[\frac{3}{(2J-1)(2J+3)}\right]^{1/2}$	$\left[\frac{3(J-1)(J+1)}{(2J-1)(2J+3)}\right]^{1/2}$
$l=J+2$	$\left[\frac{3(J+1)(J+2)}{2(2J+1)(2J+3)}\right]^{1/2}$	$-\left[\frac{2J(J+2)}{(2J+1)(2J+3)}\right]^{1/2}$	$\left[\frac{J(J-1)}{2(2J+1)(2J+3)}\right]^{1/2}$

in Table I for distances R large enough that (33) is satisfied. The diagonal energies at large R in the pure Hund's case-(e) basis (37) are simply

$$V_f = W_f^\infty + Bl_f(l_f+1) , \tag{38}$$

where W_f^∞ is the asymptotic energy. The permissible values of l_f are $l_f = J_f \pm 1$ for the 2×2 p_--parity block and $l_f = J_f$, $J_f \pm 2$ for the 3×3 p_+-parity block.

The close-coupled equations (14) can be solved just as easily using the Hund's case-(e) basis (37) as using the Hund's case-(a) basis (28), since these are obtained from each other by a unitary transformation. Equations (14b) are uncoupled at large R in a case-(e) basis, but become strongly coupled at small R. The actual numerical solutions to the equations (14) were calculated using the case-(a) matrix elements in Table I, but the amplitudes were transformed to a case-(e) basis before extracting the S matrix. Exactly the same S matrix would be obtained if the whole calculation had been carried out in case-(e) basis.

B. Radiative coupling matrix elements

The interaction between the colliding atoms and the photons is contained in the $V^{\rm rad}$ matrix elements in (14). These are calculated by taking the matrix element of (20) over the electronic-rotational basis functions. In order to use the Hund's case-(a) basis, the $\mu_0^{\rm sp}$ space-fixed projection of the dipole operator must be written in terms of the molecule-fixed projections:

$$\mu_0^{\rm sp} = \sum_{k=-1}^{1} D_{0k}^{1*} \mu_k . \tag{39}$$

The integration over rotational coordinates can be carried out analytically, and we obtain

$$V_{if}^{\rm rad} = \left[\frac{2\pi h\phi}{\lambda}\right]^{1/2} (J_f 1 J_i \mid M0M) \times (J_i p_+, \Lambda = 0 \mid\mid \mu \mid\mid J_f p_f \Lambda_f) . \tag{40}$$

The electronic-rotational reduced matrix element is

$$(J_i p_+ 0 \mid\mid \mu \mid\mid J_f p_f 0) = \left[\frac{2J_f+1}{2J_i+1}\right]^{1/2} (J_f 1 J_i \mid 000)\tau_0 \tag{41a}$$

for the $^1\Sigma$-$^1\Sigma$ transition, and

$$(J_i p_+ 0 \mid\mid , u \mid\mid J_f p_f 1) = \left[\frac{2J_f+1}{2J_i+1}\right]^{1/2} (J_f 1 J_i \mid 1,-1,0) \frac{1\pm(-1)^{J_f-J_i+1}}{\sqrt{2}} \tau_1 \tag{41b}$$

for the $^1\Sigma$-$^1\Pi$ transition. The electronic transition dipole moments are

$$\begin{aligned} \tau_0(R) &= \langle {}^1\Sigma_i \mid \mu_0 \mid {}^1\Sigma_f \rangle , \\ \tau_1(R) &= \langle {}^1\Sigma_i \mid \mu_{\pm 1} \mid {}^1\Pi_{\mp} \rangle \\ &= -\langle {}^1\Pi_{\pm 1} \mid \mu_{\pm 1} \mid {}^1\Sigma_i \rangle . \end{aligned} \tag{42}$$

The transition dipole operators are defined by

$$\begin{aligned} \mu_0 &= e\sum_n z_n , \\ \mu_{\pm 1} &= e\sum_n \frac{\mp x_n - i y_n}{\sqrt{2}} , \end{aligned} \tag{43}$$

where the summation runs over all electrons.

As long as we are only interested in the low intensity profile where the radiative S-matrix elements are linear in $\phi^{1/2}$, the M average required in (16) can be carried out in the same way as for (23). As a practical matter, the Clebsch-Gordan coefficient $(J_f 1 J_i \mid M0M)$ in (40) is replaced by its root-mean-square value $1/\sqrt{3}$ times its phase $f_\pm = \pm 1$. Thus we use

$$V_{if}^{\rm rad} = \left[\frac{2\pi h\phi}{3\lambda}\right]^{1/2} f_\pm (J_i p_i 0 \mid\mid \mu \mid\mid J_f p_f \Lambda_f) . \tag{44}$$

The expressions (41) lead to selection rules as to which possible $J_f p_f$ blocks of the final-state Hamiltonian can couple to the initial $J_i p_+$ state. The lower 2×2 p_--parity block couples only if $J_f = J_i$. The lower 3×3 p_+-parity block only couples if $J_f = J_i \pm 1$. The transitions with $J_i - J_f = -1$, 0, and $+1$, respectively, are designated P, Q, and R transitions.

The reduced electronic-rotational matrix elements (41) are shown in Table III. These radiative coupling matrix elements can also be written in a Hund's case-(e) basis by using the transformation (37) with the coefficients in Table II. These case-(e) matrix elements are also shown in Table III. These were constructed using the asymptotic relation

TABLE III. Case-(a) and -(e) radiative coupling matrix elements (for the initial state $l_i=l=J_i=J$).

Transition	case (a) $(J\|\|\mu\|\|J_f)$	Transition	case (e) $(J\|\|\mu\|\|J_f)$
		$Q(J_f=J)$	
$^1\Sigma$-$^1\Pi$	τ_1	$l_f=l+1$	$\left[\frac{J+2}{3(2J+1)}\right]^{1/2}\tau_0$
$^1\Sigma$-$^1\Delta$	0	$l_f=l-1$	$-\left[\frac{J-1}{3(2J+1)}\right]^{1/2}\tau_0$
		$P(J_f=J+1)$	
$^1\Sigma$-$^1\Sigma$	$-\left[\frac{J+1}{2J+1}\right]^{1/2}\tau_0$	$l_f=l+3$	$-\left[\frac{25(J+1)(J+2)(J+3)}{6(2J+1)(2J+3)(2J+5)}\right]^{1/2}\tau_0$
$^1\Sigma$-$^1\Pi$	$\left[\frac{J+2}{2J+1}\right]^{1/2}\tau_1$	$l_f=l+1$	$\frac{J}{2J+1}\left[\frac{J+2}{2J+5}\right]^{1/2}\tau_0$
$^1\Sigma$-$^1\Delta$	0	$l_f=l-1$	$-\frac{J-1}{2J+1}\left[\frac{J}{6(2J+3)}\right]^{1/2}\tau_0$
		$R(J_f=J-1)$	
$^1\Sigma$-$^1\Sigma$	$\left[\frac{J}{2J+1}\right]^{1/2}\tau_0$	$l_f=l+1$	$\frac{J+2}{2J+1}\left[\frac{J+1}{6(2J-1)}\right]^{1/2}\tau_0$
$^1\Sigma$-$^1\Pi$	$\left[\frac{J-1}{2J+1}\right]^{1/2}\tau_1$	$l_f=l-1$	$-\frac{J+1}{2J+1}\left[\frac{J-1}{2J-3}\right]^{1/2}\tau_0$
$^1\Sigma$-$^1\Delta$	0	$l_f=l-3$	$\left[\frac{25J(J-1)(J-2)}{6(2J+1)(2J-1)(2J-3)}\right]^{1/2}\tau_0$

$\tau_1=\tau_0/\sqrt{3}$ discussed in Sec. III D.

There are eight possible dipole-allowed transitions. The $^1\Sigma$-$^1\Delta$ transition is forbidden in Hund's case (a). However, this transition can borrow intensity from the $^1\Sigma$-$^1\Pi$ transition when the $^1\Pi$ state mixes with the $^1\Delta$ state through the electronic-rotational Born-Oppenheimer breakdown terms. At large internuclear separation where the case-(a) states are strongly mixed to give case-(e) states, all eight transitions have nonvanishing matrix elements. Note that the dipole selection rule in case (e) is $\Delta l=\pm1,\pm3$. The $\Delta l=\pm3$ transitions can occur because the electronic angular momentum L changes by two units ($^1S\rightarrow{}^1D$).

C. Born-Oppenheimer approximation

In order to compare the close-coupled profile calculated from the full Hamiltonian with the profile in the Born-Oppenheimer approximation, we will set up a simplified approximate Hamiltonian. The radiative coupling will still be included in the close-coupled scattering equations (14), but the final states will be completely decoupled.

We begin by assuming that we can ignore the off-diagonal Coriolis coupling terms in Table I. The motion in the lower state is assumed to occur only on a single Born-Oppenheimer potential curve $W_{\Lambda f}+BX_f$. We further assume that we can ignore any changes in rotational angular momentum J between initial and final states, i.e., $J_f=J_i$. Thus, the squared S-matrix element for each rotational branch scales as the case-(a) rotational factors in Table III, and the sum over branches can be found by using the root-mean-square of the matrix elements in Table III. Thus, we use $(J\|\|\mu\|\|J)=\tau_0$ for the Σ-Σ transition and $\sqrt{2}\tau_1$ for the Σ-Π transition.

These assumptions are the ones normally used in line profile theory, and were used previously to calculate the profile for collision-induced O $^1S\rightarrow$O ^1D emission in argon. The Σ-Σ and Σ-Π transitions occur independently of each other in this approximation, and are described by separate 2×2 scattering equations. (A single 3×3 set of equations could also be used, but the lower $^1\Sigma$ and $^1\Pi$ states would remain uncoupled.) The Born-Oppenheimer Hamiltonian with the $\Delta J=0$ approximation is shown in

Table IV. The only coupling is radiative coupling.

D. Potentials and transition moments

The specification of the scattering Hamiltonian in (14) will be complete once we show the molecular potentials $W_\Lambda(R)$ and transition moments $\tau_\Lambda(R)$ which were actually used. These have been described previously.[25,31] The potentials were constructed by adding the dispersion potential through $-C_{10}/R^{10}$ to the exchange-overlap repulsion energy calculated with multiconfiguration self-consistent-field (MCSCF) wave functions. The potentials are parametrized by the function

$$W(R)=Ae^{-\alpha R}+W_{\rm disp}(R)+W^{\infty}\ , \tag{45}$$

where A and α are obtained by fitting the MCSCF data. The dispersion energy is

$$W_{\rm disp}(R)=-\frac{C_6}{R^6}-\frac{C_8}{R^8}-\frac{C_{10}}{R^{10}}\ . \tag{46}$$

The zero of energy (including the radiation field energy) is chosen to be the asymptotic atoms in their initial electronic states, $W_i^{\infty}=0$. Thus, $W_f^{\infty}=\Delta$ for the final states, with Δ given by Eq. (3). The potential parameters are shown in Table V and the potentials are illustrated in Fig. 1.

The quadrupole-induced dipole transition moments have the long-range form

$$\tau_0=\frac{T_4}{R^4}\ ,\qquad \tau_1=\frac{1}{\sqrt{3}}\frac{T_4}{R^4}\ , \tag{47}$$

TABLE IV. Born-Oppenheimer Hamiltonian with $\Delta J=0$ $[X\equiv J(J+1)]$.

	$^1\Sigma$-$^1\Sigma$ transition	
	$^1\Sigma_i$	$^1\Sigma_f$
$^1\Sigma_i$	$W_{0i}+BX$	$\left[\frac{2\pi h\phi}{3\lambda}\right]^{1/2}\tau_0$
$^1\Sigma_f$	$\left[\frac{2\pi h\phi}{3\lambda}\right]^{1/2}\tau_0$	$W_{0f}+BX$
	$^1\Sigma$-$^1\Pi$ transition	
	$^1\Sigma_i$	$^1\Pi_f$
$^1\Sigma_i$	$W_{0i}+BX$	$\left[\frac{2\pi h\phi}{3\lambda}\right]^{1/2}\sqrt{2}\tau_1$
$^1\Pi_f$	$\left[\frac{2\pi h\phi}{3\lambda}\right]^{1/2}\sqrt{2}\tau_1$	$W_{1f}+BX$

TABLE V. Potential parameters for ArO.

Asymptote	State	MCSCF energy $A_\Lambda(\text{cm}^{-1})$	$\alpha_\Lambda(a_0^{-1})$
$^1S+^1S$	$^1\Sigma^+$	4.280×10^7	2.042
$^1S+^1D$	$^1\Sigma^+$	5.102×10^7	2.211
$^1S+^1D$	$^1\Pi$	3.116×10^7	2.018
$^1S+^1D$	$^1\Delta$	4.456×10^7	1.966
		Dispersion energy	
$^1S+^1S$	$^1\Sigma^+$	$C_6=6.672\times10^6\ \text{cm}^{-1}a_0^6$	
		$C_8=1.221\times10^8\ \text{cm}^{-1}a_0^8$	
		$C_{10}=2.308\times10^9\ \text{cm}^{-1}a_0^{10}$	
$^1S+^1D$	$^1\Sigma^+$	$W_{\rm disp}=0.9310W_{\rm disp}(^1S+^1S)$	
$^1S+^1D$	$^1\Pi$	$W_{\rm disp}=0.9555W_{\rm disp}(^1S+^1S)$	
$^1S+^1D$	$^1\Delta$	$W_{\rm disp}=1.0290W_{\rm disp}(^1S+^1S)$	

where $T_4=37.8ea_0$.[25] The $^1\Sigma$-$^1\Sigma$ transition moment τ_0 departs from the long-range form (47) for $R<7.5a_0$, so that it is necessary to use the *ab initio* calculated transition moment for small R. Thus, the long-range form for τ_1 was used at all R, whereas for τ_0 a tensioned cubic spline fit of the moment calculated by Dunning and Hay[44] was smoothly joined to the long-range form (47) at $R=7.5a_0$. The transition moments are shown in Fig. 2.

The previous calculation[25,31] assumed the same dispersion energy for the initial and final states since the O ^1S and O ^1D polarizabilities are nearly identical.[45] In order to avoid unrealistic asymptotic behavior of the potentials, an estimate has been made of the difference in dispersion energy between initial and final states and of the Λ dependence of

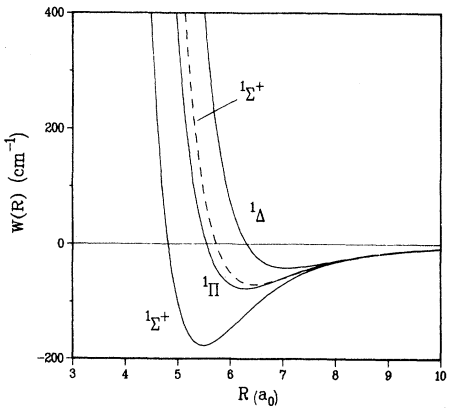

FIG. 1. Born-Oppenheimer potential energy curves $W(R)$ for ArO corresponding to the parameters in Table V for $\Delta=0$. Dashed curve shows the initial $^1\Sigma^+$ state which correlates with O ^1S, whereas the solid curves correlate with O ^1D.

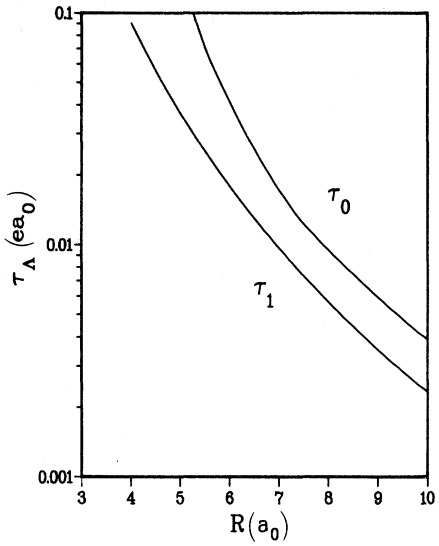

FIG. 2. Dipole electronic transition moments for the ArO $^1\Sigma$-$^1\Sigma$ and $^1\Sigma$-$^1\Pi$ transitions.

C_6 for the states from the O ^1D asymptote. We construct the following approximate model for the dispersion differences based on the small differences between the calculated oxygen static dipole polarizabilities $\alpha(L,\Lambda)$:

$$\overline{C_6}(^1D)=0.98C_6(^1S) \tag{48}$$

since $\bar{\alpha}(^1D)$ is 2% less than $\alpha(^1S)$[45] (the bar means spherical average);

$$C_6(^1D,\ \Lambda=2)-C_6(^1D,\ \Lambda=0)=0.1\overline{C_6}(^1D)\ , \tag{49}$$

chosen as an approximate model of the difference because of the 13% difference in static polarizabilities[45]; and

$$C_6(^1D,\ \Lambda=1)-C_6(^1D,\ \Lambda=0)$$
$$=\frac{1}{L^2}[C_6(^1D,\Lambda=2)-C_6(^1D,\Lambda=0)]\ , \tag{50}$$

derived by applying the Wigner-Eckart theorem to the definition of C_6. It we assume that the same relations apply to the total dispersion energy we arrive at the magnitudes in Table V. Using these slightly modified long-range potentials does not change any of the results of Julienne,[31] as discussed below.

IV. RESULTS OF CALCULATION

A. Numerical methods

The close-coupling code used in these calculations is based on Gordon's algorithm[46] and has been described previously.[47] Care was taken in computing the numerical propagation step size to insure that accuracy is maintained in the calculated S matrix. The coupled equations (14) were solved numerically using the Hamiltonian matrix elements described in Sec. III. A separate calculation was made for each initial kinetic energy ϵ, initial total molecular angular momentum J, and detuning $\Delta=\epsilon-\epsilon_f$. The strength of the radiation field was arbitrarily chosen to be 10^4 W cm^2. The reduced free-free matrix elements $(\epsilon J||\mu||\epsilon_f J_f)$ were found from the numerically calculated radiative S-matrix elements using (26). Summing these over all contributing initial J values gives the dipole strength function $D_\epsilon(\Delta)$ (25), which is numerically accurate to about 0.1%. The profile function $K(\Delta,T)/\phi$ is found by thermally averaging the strength function in accordance with (24). The profile function reported here is that for spontaneous emission, $k_{se}(\Delta,T)$, defined by Eq. (9). All energies are expressed in cm^{-1}, and the profile k_{se} is given in cm^3 (equivalent to cm^3 sec^{-1} Hz^{-1}, or a rate coefficient per unit frequency interval).

Two distinct types of calculations were carried out, in order to provide a basis of comparison.

(1) The profile was calculated using the Born-Oppenheimer approximation for the final states. Two separate 2×2 scattering calculations were carried out using the Hamiltonians in Table IV. This defines two separate dipole strength functions, $D_\epsilon^\Sigma(\Delta)$ and $D_\epsilon^\Pi(\Delta)$, for the respective Σ-Σ, and Σ-Π transitions. The total Born-Oppenheimer dipole strength is

$$D_\epsilon^{BO}(\Delta)=D_\epsilon^\Sigma(\Delta)+D_\epsilon^\Pi(\Delta)\ . \tag{51}$$

The corresponding thermally averaged profiles, k^Σ, k^Π, and k^{BO}, are similarily defined.

(2) The profile was calculated using the final-state close-coupled Hamiltonian of Table I. Since final states of *different* J_f are not coupled except through negligible second-order radiative couplings, the radiative selection rules permit the calculation to be broken into three separate scattering calculations in accordance with Table III. One is a set of three coupled equations comprised of the initial state and the $^1\Pi$ and $^1\Delta$ final states of p_- parity with $J_f=J$; the other two are sets of four coupled equations comprised of the initial state and the $^1\Sigma$,

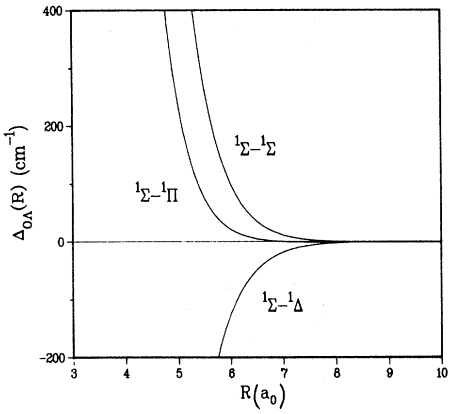

FIG. 3. Difference potentials $\Delta_{0\Lambda}$ between the initial $^1\Sigma^+$ state and final Λ states.

$^1\Pi$, and $^1\Delta$ final states of p_+ parity with $J_f = J \pm 1$. These Q, P, and R calculations define three dipole strength functions, D^Q, D^P, and D^R, and the total close-coupled dipole strength function is

$$D_\epsilon^{CC}(\Delta) = D_\epsilon^Q(\Delta) + D_\epsilon^P(\Delta) + D_\epsilon^R(\Delta) . \quad (52)$$

The case-(a) Hamiltonian matrix elements of Tables I and III were used in the numerical matrices. The radiative S-matrix elements were evaluated by projecting the asymptotic solutions onto the case-(e) basis, as discussed previously. Identical results would be obtained if the case-(e) basis were used throughout.

B. Born-Oppenheimer profile

A frequently used approximation in line profile theory is the classical Franck-Condon principle, according to which a photon transition of frequency ν occurs at an internuclear separation R where the difference between initial and final potential equals the photon energy $h\nu$. In our notation, this occurs at the R where $\Delta = W_{0i} - W_{\Lambda f}$, that is, where the initial and final molecule-field potentials cross. The difference potential $\Delta_{0\Lambda} = W_{0i} - W_{\Lambda f}$ for ArO, with the parameters in Table V, are shown in Fig. 3. The Σ-Σ and Σ-Π difference potentials are positive, except they become slightly negative ($-2 \leq \Delta_{0\Lambda} \leq 0$ cm^{-1}) at long range since the lower potentials are asymptotically less attractive than the upper. Thus, the Born-Oppenheimer, classical Franck-Condon picture leads us to expect a peak in the profile near $\Delta = 0$, a long quasistatic wing for blue detuning where $\Delta = \Delta_{0\Lambda}(R)$ is satisfied, and a rapidly decaying antistatic wing for red detuning where $\Delta = \Delta_{0\Lambda}(R)$ cannot be satisfied.

This expectation is verified by our earlier quantum-mechanical profile calculation, for which the free-free integrals, $\langle \epsilon J \,|\, \mu(R) \,|\, \epsilon_\Lambda J \rangle$, were explicitly evaluated with Born-Oppenheimer wave functions and assuming an R^{-4} variation of the electronic transition moments for all R.[25] The quasistatic expression for the profile,

$$k_{se}^{QS}(\Delta) = \frac{256\pi^5}{3\lambda^3} \left[\frac{R_0^2 \tau_0^L}{\left| \frac{d\Delta_{00}}{dR} \right|_{R_0}} + 2 \frac{R_1^2 \tau_1^2}{\left| \frac{d\Delta_{01}}{dR} \right|_{R_1}} \right] \quad (53)$$

was shown to agree well with the quantum-mechanical profile in the blue wing.[31] Gallagher and Holstein have shown that their Fourier-transform technique, which relies on the Born-Oppenheimer approximation but not the classical Franck-Condon approximation, reproduces our calculated antistatic red wing.[22] Both the red and blue wings show significant discrepancies with the measured profile.[25] To obtain quantitative agreement of the calculated blue-wing profile with the measured profile required using the proper short-range form of the transition moments from *ab initio* calculations. The quasistatic formula (53) with the transition moments discussed in this paper (see Sec. III D) predicted a quasistatic blue wing which agrees with the measured profile within 20% for $50 < \Delta < 600$ cm^{-1}.[31] The red-wing calculations were not repeated with the new transition moments in this previous work.

The present paper only studies the free-free contribution to the profile. This is by far the dominant part in the central region of the profile. Our previous quantum-mechanical calculations showed that free-bound emission was important for large blue detuning, accounting for about half of the total profile for $\Delta > 200$ cm^{-1}. However, free-bound emission was found to be negligible ($< 3\%$) for $\Delta < 50$ cm^{-1}. Bound-bound emission contributes only about 6% of the total decay coefficient (i.e., area under the profile function). The quasistatic expression accounts for emission from all parts of phase space, including bound, quasibound, and free emission.

The scattering technique proposed in this paper for calculating the profile was first checked by calculating the reduced matrix elements $(\epsilon J || \mu || \epsilon_\Lambda J)$ for the same potentials and transition moments as in our original calculation. Perfect agreement was found with the previously calculated overlap in-

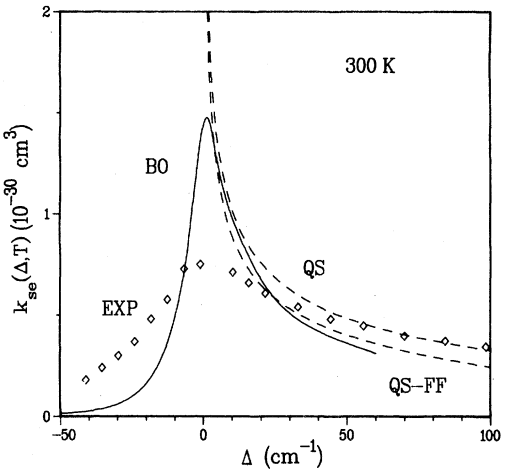

FIG. 4. Calculated thermally averaged Born-Oppenheimer profile function $k_{se}^{BO}(\Delta,T)$ for ArO at 300 K. Solid line shows the quantum-mechanical profile (BO) and the dashed lines show the total quasistatic profile (QS) as well as the free-free (FF) contribution to the quasistatic profile (QS-FF). Points ($\diamond$) show the experimental profile function.

tegrals $\langle \epsilon J \mid \tau_\Lambda \mid \epsilon_\Lambda J \rangle$. Approximately the same amount of computer time was required for the scattering and direct-integration methods.

The calculation of the Born-Oppenheimer profile was repeated with the use of the potentials and transitions moments in Table V. The resulting thermally averaged profile at 300 K is compared to the measured profile in Fig. 4. None of our previous conclusions are changed by this calculation. The 20% agreement between the measured and quasistatic profile is maintained for the far-blue wing ($\Delta > 50$ cm^{-1}). The strong disagreement in the shape of the peak and red-wing falloff is not removed; Calculation and measurement differ by a factor of 2 at the peak and by a factor of 6 by $\Delta = -50$ cm^{-1}. The figure also shows the total and free-free quasistatic profiles. The quantum free-free profile makes typical oscillations about the quasistatic envelop.

The experimental emission profile[36,37] was measured by recording on film the emission from an electron beam excited Ar-O_2 mixture containing several Torr of O_2 and several atmospheres of Ar. Under these conditions, the collision-induced molecular dipole emission completely dominates the weak atomic $^1S \rightarrow {}^1D$ quadrupole emission.[21] The linearized film response determined the shape of the emission profile with a 0.2-nm $\sim$6-cm^{-1} resolution. The profile was placed on an absolute scale by normalizing the area under this shape function to the measured total decay coefficient

$$K_{se} = \int_0^\infty k_{se}(v)dv \tag{54}$$

taken to be 4.5×10^{-18} cm^{3}sec^{-1}. The calculated value of K_{se} at 300 K is 4.2×10^{-18} cm^{3}sec^{-1},[31] which is in excellent agreement with the range of measured values 3.9×10^{-18} to 5.1×10^{-18} cm^{3}sec^{-1}.[32–35] An estimated uncertainty of $\pm20\%$ is not unreasonable for the experimental profile function. The temperature of the mixture following e-beam deposition was not measured, but is probably between 300 and 400 K. In any case, no realistic assumption about the temperature can remove the discrepancy between calculated and measured profiles.

C. Close-coupled profile

The calculated quantum-mechanical close-coupled dipole strength function $D_\epsilon^{CC}(\Delta)$ is shown in Fig. 5 for a collision kinetic energy $\epsilon = 300$ cm^{-1}. This is compared with the quantum-mechanical and quasistatic Born-Oppenheimer strength functions for the same collision energy. The two quantum-mechanical functions give essentially the same blue wing for $\Delta > 30$ cm^{-1}, and both are oscillating about the quasistatic function. There is a dramatic difference between the close-coupled and Born-Oppenheimer quantum-mechanical profiles. The closed-coupled (CC) profile has decreased in peak

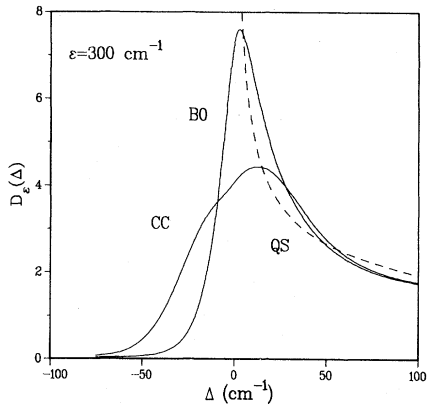

FIG. 5. Calculated line strength function $D_\epsilon(\Delta)$ of Eq. (25) for an initial-state center-of-mass kinetic energy $\epsilon = 300$ cm^{-1}. (For comparison the thermal energy $kT = 209$ cm^{-1} at 300 K.) This function is expressed in units of $10^{-4}e^2a_0^2$ energy^{-2} with energy in cm^{-1} and $ea_0 = 1$ corresponding to atomic units. Close-coupled, Born-Oppenheimer, and quasistatic profiles are shown.

magnitude and increased red-wing intensity relative to the BO profile.

The CC and BO thermally averaged profiles are compared to the measured profile in Figs. 6 and 7. The former is a linear plot emphasizing the central region, whereas the latter is a logarithmic plot emphasizing the wing behavior. The CC profile is in remarkably good agreement with the measured profile. The difference between the CC and BO calculations is especially evident in the red-wing dropoff in Fig. 7. It is evident that the normal assumptions of line profile theory fail for this problem and that a closed-coupled description of the final states is both necessary and adequate to remove the discrepancies.

It is now highly desirable to try to find some understanding of the reasons for the differences between the CC and BO profiles. In short, the major reason is that a large part of the peak and red-wing region originates from moderately large internuclear separations where the electronic angular momentum is decoupled from the rotating molecular axis, i.e., the case-(a) BO states of fixed Λ are strongly mixed by the Coriolis interaction. Considerable insight into this effect can be gained by introducing for the final states from $O\,^1D$ the adiabatic-electronic-rotational (AER) states defined by Mies.[38] These states are the ones which continuously diagonalize the electronic-rotational Hamiltonian (Table I) as a function of R

$$\underline{V}^{Jp}_{\rm AER}=\underline{U}^{Jp}(R)\underline{V}^{Jp}_{\rm BO}(R)\underline{\tilde{U}}(R)\ , \tag{55}$$

where $\underline{V}_{\rm AER}$ is diagonal. The AER electronic-rotational basis functions are

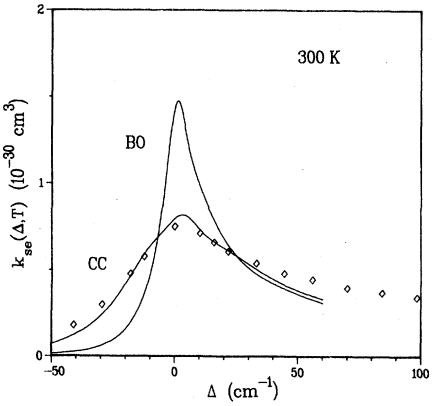

FIG. 6. Calculated close-coupled and Born-Oppenheimer thermally averaged ArO profile functions at 300 K (solid lines) compared to the experimental profile ($\Diamond$).

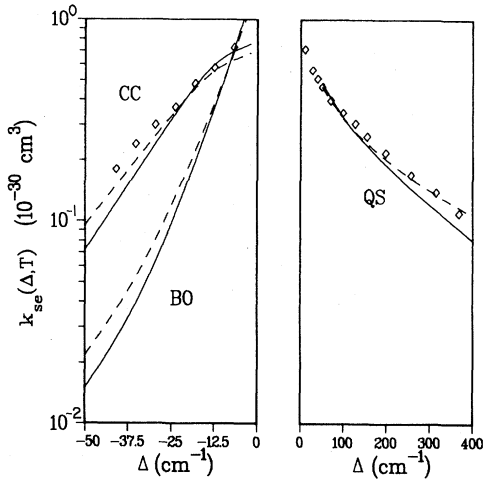

FIG. 7. Red- and blue-wing ArO profiles. Points give the experimental profile. Solid and dashed lines give the calculated profiles for 300 and 400 K, respectively. CC and BO profiles are shown for the red wing, whereas only the total quasistatic profile is shown for the far-blue wing.

$$\underline{\psi}^{JMp}_{\rm AER}=\underline{U}^{Jp}(R)\underline{\psi}^{JMp}_{\rm BO}\ , \tag{56}$$

where $\psi_{\rm BO}$ represents the vector of BO electronic-rotational basis functions (28). The AER functions approach pure case-(a) functions at small R and pure case-(e) functions at large R. They switch smoothly from one to the other over some intermediate range of distances near where (33) is an equality.

Figure 8 shows the projection of the middle AER function of the 3×3 p_+ parity block on the case-(a) $^1\Pi p_+$ basis function. The projection approaches

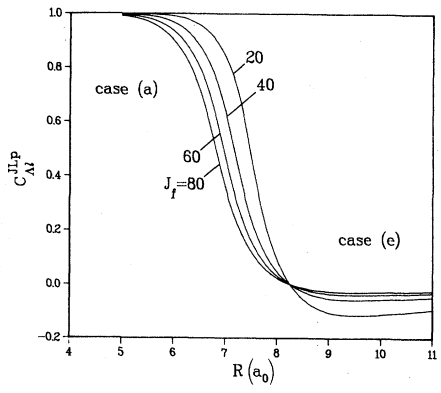

FIG. 8. Projection of the middle AER root of the 3×3 p_+ electronic-rotational Hamiltonian on the pure case-(a) $^1\Pi p_+$ basis function, shown for several values of total lower state angular momentum J_f.

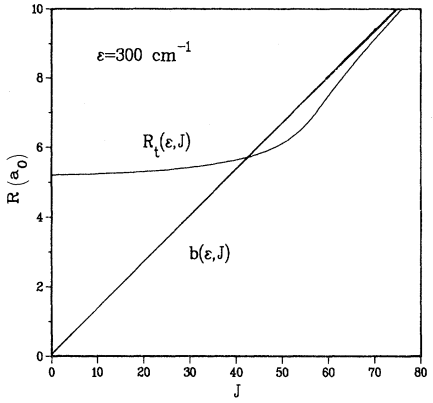

FIG. 9. Upper state classical turning point $R_t(\epsilon,J)$ and impact parameter $b(\epsilon,J)$ as a function of J for $\epsilon=300$ cm^{-1}.

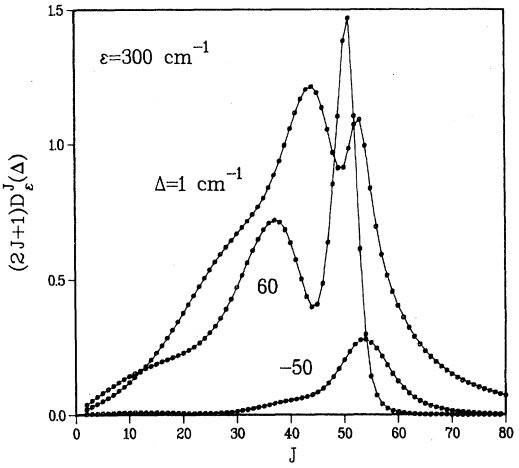

FIG. 10. Contribution $(2J+1)D^J_\epsilon(\Delta)$ to the profile function (25) as a function of J for $\epsilon=300$ cm^{-1} and detunings $\Delta=-50$, 1, and 60 cm^{-1}. Units are the same as in Fig. 5.

the case-(a) limit of unity at small R and the case-(e) limit $\approx -\sqrt{3}/2J$ at large R (see Table II). Similar switching between case-(a) and case-(e) limits as a function of R would be illustrated by any of the other eight possible $(e)\rightarrow(a)$ projections in the p_+ block or by the four projections of the p_- block. The figure shows that the departure of the mixing coefficient from its case-(a) value is 10% or less when $R \lesssim 6.8a_0$ for $J=20$ and $R \lesssim 6.2a_0$ for $J=60$. The switching to the case-(e) asymptotic limit is nearly complete for $R \gtrsim 8a_0$. The region $6.5 \lesssim R \lesssim 8a_0$ is a switching zone where intermediate coupling applies.

Figure 9 shows the classical turning point $R_t(\epsilon,J)$ of the initial $^1\Sigma^+$ centrifugal potential as a function of J for a center-of-mass collision kinetic energy of $\epsilon=300$ cm^{-1}. The figure also shows the impact parameter associated with each J, $b(\epsilon,J)=\hbar(J+\frac{1}{2})/\sqrt{2\mu\epsilon}$, which is the classical turning point of the centrifugal potential for noninteracting particles colliding with energy ϵ and angular momentum J. We see from Figs. 8 and 9 that case (a) applies to the lower states at the position of the initial-state turning point when $J \lesssim 50$ and case (e) applies when $J \gtrsim 60$ for $\epsilon=300$ cm^{-1}. The upper turning point lies in the lower state switching region when $50 \lesssim J \lesssim 60$.

Figure 10 shows the contribution

$$(2J+1)D^J_\epsilon(\Delta)=(2J+1)\sum_f |(\epsilon J||\mu||\epsilon_f J_f)|^2 \tag{57}$$

to the profile [see Eq. (25)] as a function of J for $\epsilon=300$ cm^{-1} for red, peak, and blue detunings. Most of the profile for blue detuning comes from impact parameters (angular momenta) for which the distance $R_{\rm CFC}$ at which the classical Franck-Condon (CFC) principle is satisfied is accessible during the collision. For the case $\Delta=60$ cm^{-1} illustrated in the figure, $R_{\rm CFC}=6.26a_0$ for the Σ-Σ transition, which lies in the classically inaccessible region of the potential for $J>51$ when $\epsilon=300$ cm^{-1}. There is a rapid drop-off in $D^J_\epsilon(\Delta=60$ cm$^{-1})$ when $J>51$. Since this profile originates from regions of internuclear separation which are dominantly Hund's case (a), it is not surprising that the BO profile agrees well with the CC profile for blue detuning (see Fig. 5). The agreement improves with further blue detuning.

The situation is quite different for the peak and red detuning regions of the profile. Figure 10 shows that a substantial part of the profile, respectively, 33% and 67% for $\Delta=1$ and -50 cm^{-1}, comes from large impact parameters $J>50$ where the lower states are dominantly case (e) or switching towards case (e) at classically accessible distances for motion on the initial potential. Therefore, we should not expect the Born-Oppenheimer approximation to give a correct description of the profile peak or red wing.

The closed-coupled wave function can be expanded in the AER basis as well as a case-(a) or case-(e) basis. Mies has shown that the close-coupled amplitudes F [see Eq. (13)] take on the following form in an AER expansion[38]:

$$\underline{F}^{\rm AER}(R)=[\underline{f}^0(R)+\underline{g}^0(R)\underline{r}(R)]\underline{N}(R)\ , \tag{58}$$

where $\underline{f}^{(0)}$ and $\underline{g}^{(0)}$ are diagonal matrices whose elements are the respective regular and irregular solutions of the *uncoupled* Schrödinger equations for the diagonalized potentials of (55). $\underline{N}$ is an R-dependent normalization matrix, and the R-dependent matrix $\underline{r}$ describes the inelastic scattering among the AER states. The AER theory gives coupled first-order nonlinear differential equations for $\underline{r}$ and $\underline{N}$.

The AER theory gives a series of approximations for $\underline{r}$.[38,48] The simplest possible approximation is to ignore inelastic couplings among the AER states reflected in the $\underline{gr}$ term and approximate $\underline{F}^{\mathrm{AER}}$ by the uncoupled regular solutions $\underline{f}^{0}$ of the diagonal AER potentials and a constant diagonal normalization matrix. When the final-state close-coupled wave functions are decoupled in this way, the unitary transformation $\underline{U}$ applied to the case-(a) transition moments in Table III yields eight distinct transition moments corresponding to the eight possible transitions in Table III. These AER transition dipoles correlate at small R with the case-(a) expressions in the table and at large R with the case-(e) expressions. Since the final states are decoupled, the profile can be found by eight separate 2×2 scattering calculations in which the initial state is coupled radiatively to each of the possible final decoupled AER states. This gives the AER approximation to the profile

$$D_{\epsilon}^{\mathrm{AER}}(\Delta)=\sum_{f=1}^{8} D_{\epsilon}^{f,\mathrm{AER}}(\Delta)\ . \tag{59}$$

Since inelastic coupling in the $(a)\leftrightarrow(e)$ switching region is ignored in this zeroth-order AER approximation, this approximation is inappropriate if we wanted to predict, for example, the detailed m_j distribution of the final $^1D_2$ products. A sudden rather than "adiabatic" correlation with the final-state distribution is probably more realistic.[28,30] However, the decoupling approximation may not be so bad for the total profile where we sum over all possible final states. Figure 11 shows a comparison of the close-coupled and the AER approximation for $D_{\epsilon}(\Delta)$ for $\epsilon=300\ \mathrm{cm}^{-1}$. We see that the AER profile reproduces the qualitative features of the peak and red-wing regions of the profile. In the blue wing the CC, AER, and BO profiles all coincide. The figure also shows the breakdown of the total profile into its separate contributions for P-, Q-, and R-type transitions. The AER theory also reproduces the qualitative differences among these transitions with different ΔJ. This separation of P, Q, and R contributions to the profile is responsible for

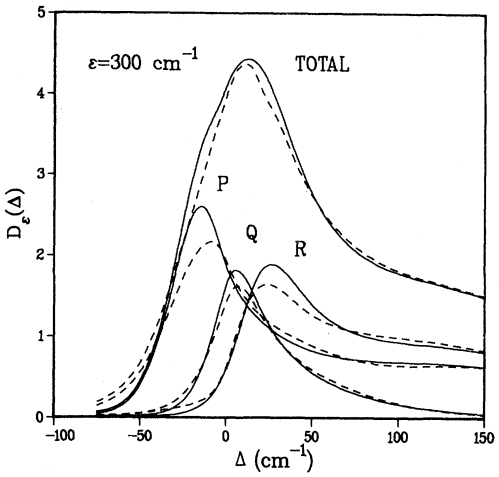

FIG. 11. Total CC (solid curves) and AER (dashed curves) profiles $D_{\epsilon}(\Delta)$ for $\epsilon=300\ \mathrm{cm}^{-1}$. Units are the same as in Fig. 5. Individual contributions from the P, Q, and R types of transitions are shown. These partial profiles have been summed over all possible final states within each ΔJ class.

the small shoulder on the CC profile in Figs. 5, 6, and 11.

There are two significant aspects of the AER profile which account for its main qualitative differences with the BO profile. These provide a qualtitative rationalization as to why the CC and BO profiles are so different.

(1) For the range of internuclear separation where switching from cases (a) to (e) occurs, the $^1\Delta$ state mixes with the $^1\Pi$ and $^1\Sigma$ states through Coriolis coupling, so that the $^1\Sigma$-$^1\Delta$ forbidden transition borrows intensity from the allowed $^1\Sigma$-$^1\Sigma$ and $^1\Sigma$-$^1\Pi$ transitions. Since the $^1\Sigma$-$^1\Delta$ difference potential satisfies the classical Franck-Condon principle for red detuning (see Fig. 3), this mixing shifts intensity from blue to red. The existence of this mixing for the larger J's contributing to the peak and red-wing part of the profile is evident from Figs. 8—10.

(2) In the case-(e) limit the nuclear angular momentum l necessarily changes by at least one unit. (See Table III. This is not true, in general, but is true for $^1S\rightarrow{}^1D$ transitions induced by an ^1S atom.) Therefore, if a transition occurs in the case-(e) region, the change in the centrifugal potential $Bl(l+1)$ contributes to the difference potential. The effect is not negligible, due to the large values of l. The strongest case-(e) P transitions have $l-l_f=-1$ and -3, and the strongest R transitions have $l-l_f=1$ and 3. The Q transitions are of comparable intensity with $l-l_f=\pm1$. The approximate change in centrifugal potential energy for a change

Δl in l is $2B\,\Delta l$. If we assume an impact parameter $b=6.6a_0$ corresponding to $\epsilon=300$ cm^{-1}, $l=50$, then $2B\,\Delta l$ is ± 12 cm^{-1} for $\Delta l=\pm 1$ and ± 36 cm^{-1} for $\Delta l=\pm 3$. Thus, we expect the P-block profile to shift several cm^{-1} to the red and the R-block profile to shift several cm^{-1} to the blue. This is what is observed to occur in both the CC and AER profiles in Fig. 11.

D. Summary

We have shown that the closed-coupled theory of atomic scattering in a radiation field gives a technique for calculating atomic line profiles. The method applies to that part of the profile which can be described by single binary collisions, i.e., to the whole profile for asymptotically forbidden laser-switched collisions and to the profile wings of asymptotically allowed transitions. The validity of the distorted-wave approximation for weak radiative coupling permits us to express the profile in terms of generalized close-coupled reduced free-free dipole matrix elements defined in terms of the radiative S-matrix elements calculated for scattering in a radiation field. The method gives a powerful tool for studying intrinsic nonadiabatic effects due to the failure of the Born-Oppenheimer approximation.

The Hund's case-$(e)\leftrightarrow(a)$ switching which we have studied here in detail is a general phenomenon which will *always* be present whenever one of the asymptotic atomic states is nondegenerate.[28–30] During the course of a collision, the electronic angular momentum is initially quantized in a space-fixed coordinate frame, but becomes coupled to the rotating molecular axis as the atoms approach each other, and again becomes decoupled as the atoms separate. When the spin does not vanish, the transition can be $(e)\leftrightarrow(c)$ or even $(e)\rightarrow(c)\rightarrow(a)\rightarrow(b)$,[48] where the letters designate the standard Hund's cases.[42] The Born-Oppenheimer approximation normally made in line profile theory assumes that the absorption or emission of a photon can be described in terms of motion on isolated initial and final Born-Oppenheimer potential curves.[27] The question for line profile theory which is raised by the work reported here is whether use of the Born-Oppenheimer approximation is always justified.

Our specific calculations on the oxygen-argon system shows a clear example where the Born-Oppenheimer approximation fails asymptotically and the $(e)\leftrightarrow(a)$ switching plays a dominant role in determining the profile. In order to answer the question as to the importance of this effect for other collision partners, it is necessary to examine the splittings of the Born-Oppenheimer molecular potentials originating from any degenerate asymptotes relative to the Coriolis coupling terms which always dominate asymptotically. If case-(e) or intermediate coupling is implied for the dominant large impact parameters, then use of the Born-Oppenheimer approximation may be expected to lead to errors in the profile.

Our calculations in progress on

$$\mathrm{Sr}+\mathrm{Ar}+nh\nu\rightarrow\mathrm{Sr}\,{}^1P_{jm_j}+\mathrm{Ar}+(n-1)h\nu$$

show that a proper treatment of the $(a)\leftrightarrow(e)$ switching is required in order to understand the data on polarized emission versus detuning.[8] The potential parameters used for a Born-Oppenheimer semiclassicl calculation of the profile for the laser-switched collision[17]

$$\mathrm{Sr}\,{}^1P+\mathrm{Ca}\,{}^1S+nh\nu\rightarrow\mathrm{Sr}\,{}^1S+\mathrm{Ca}\,4p^2\,{}^1S+(n-1)h\nu$$

predict that the Coriolis coupling energy and the estimated splitting of the ${}^1\Sigma$ and ${}^1\Pi$ potentials from the ${}^1P+{}^1S$ asymptote are both on the order of 3 cm^{-1} at the Weisskopf radius, $R=25a_0$. Since the full width at half maximum of the calculated asymmetric profile[17,22] was found to be about a factor of 2 smaller than observed,[3] the additional broadening which we expect due to $(e)\leftrightarrow(a)$ switching may help to resolve some of the discrepancy. However, the magnitude of any nonadiabatic effects can only be determined by an actual close-coupling calculation. Approximations in the potential model probably also contribute to this discrepancy. However, we are led to suggest that nonadiabatic effects due to $(e)\leftrightarrow(a)$ switching cannot be safely neglected, in general, for laser-switched collisions if a quantitative treatment of the profile is desired.

The zeroth-order AER approximation which decouples the final states helps give insight into the origin of the differences between the close-coupled and Born-Oppenheimer profile. The AER profile for our model problem agrees reasonably well with the close-coupled profile, in spite of neglecting strong inelastic couplings among AER states. Although this AER treatment retains the simplicitly of radiatively coupling only two states at a time, there is a considerable increase in complexity over the Born-Oppenheimer treatment, since each rotational transition must be calculated separately.

[1]S. E. Harris and D. B. Lidlow, Phys. Rev. Lett. 33, 674 (1974); 34, 172(E) (1975).
[2]D. B. Lidlow, R. W. Falcone, J. F. Young, and S. E. Harris, Phys. Rev. Lett. 36, 462 (1976).
[3]R. W. Falcone, W. R. Green, J. C. White, J. F. Young, and S. E. Harris, Phys. Rev. A 15, 1333 (1977).
[4]W. R. Green, J. Lukasik, J. R. Willison, M. D. Wright, J. F. Young, and S. E. Harris, Phys. Rev. Lett. 42, 970 (1979).
[5]J. C. White, R. R. Freeman, and P. F. Liao, Opt. Lett. 5, 120 (1980).
[6]P. Cahuzak and P. E. Toschek, Phys. Rev. Lett. 40, 1087 (1978).
[7]J. L. Carlsten, A. Szöke, and M. G. Raymer, Phys. Rev. A 15, 1024 (1977).
[8]P. Thomann, K. Burnett, and J. Cooper, Phys. Rev. Lett. 45, 1325 (1980).
[9]I. H. Zimmerman, J. M. Yuan, and T. F. George, J. Chem. Phys. 66, 2638 (1977).
[10]P. L. DeVries, M. S. Mahlab, and T. F. George, Phys. Rev. A 17, 546 (1978).
[11]P. L. DeVries and T. F. George, Mol. Phys. 36, 151 (1978); 38, 561 (1979); Phys. Rev. A 18, 1751 (1978).
[12]F. H. Mies, in *Theoretical Chemistry: Advances and Perspectives,* edited by D. Henderson (Academic, New York, 1981), Vol. 6B, pp. 127–198.
[13]L. I. Gudzenko and S. I. Yakovlenko, Zh. Eksp. Teor. Fiz. 62, 1686 (1972) [Sov. Phys.—JETP 35, 877 (1972)].
[14]N. M. Kroll and K. M. Watson, Phys. Rev. A 13, 1018 (1976).
[15]A. M. F. Lau, Phys. Rev. A 13, 139 (1976); 14, 279, (1976).
[16]A. M. F. Lau and C. K. Rhodes, Phys. Rev. A 15, 1570 (1977).
[17]S. E. Harris and J. C. White, IEEE J. Quantum Electron. QE-13, 972 (1977).
[18]J. M. Yuan, T. F. George, and F. J. McLafferly, Chem. Phys. Lett. 40, 163 (1976).
[19]J. M. Yuan, T. R. Laing, and T. F. George, J. Chem. Phys. 66, 1107 (1977).
[20]J. C. Light and A. Szöke, Phys. Rev. A 18, 1363 (1978).
[21]P. S. Julienne, J. Appl. Phys. 48, 4140 (1977).
[22]A. Gallagher and T. Holstein, Phys. Rev. A 16, 2413 (1977).
[23]K. M. Sando and J. Wormhoudt, Phys. Rev. A 7, 1889 (1973).
[24]A. Dalgarno and K. M. Sando, Comments At. Mol. Phys. 4, 29 (1973).
[25]P. S. Julienne, M. Krauss, and W. Stevens, Chem. Phys. Lett. 38, 374 (1976).
[26]P. S. Herman and K. M. Sando, J. Chem. Phys. 68, 1163 (1978).
[27]J. Szudy and W. E. Baylis, J. Quant. Spectrosc. Radiat. Transfer 15, 641 (1975).
[28]W. R. Thorson, J. Chem. Phys. 50, 1702 (1969).
[29]F. H. Mies, Mol. Phys. 41, 953 (1980).
[30]J. Delos, Rev. Mod. Phys. 53, 287 (1981).
[31]P. S. Julienne, J. Chem. Phys. 68, 32 (1978).
[32]D. L. Cunningham and K. C. Clark, J. Chem. Phys. 61, 1118 (1974).
[33]A. Corney and O. M. Williams, J. Phys. B 5, 686 (1972).
[34]G. Black, R. L. Sharpless, and T. G. Slanger, J. Chem. Phys. 63, 4564 (1975); 4551 (1975).
[35]K. H. Welge and R. Atkinson, J. Chem. Phys. 64, 531 (1976).
[36]J. R. Murray and C. K. Rhodes, J. Appl. Phys. 47, 5041 (1976).
[37]H. T. Powell and J. R. Murray (private communication).
[38]F. H. Mies, Mol. Phys. 41, 973 (1980).
[39]F. H. Mies, J. Chem. Phys. 51, 787 (1969).
[40]M. E. Rose, *Elementary Theory of Angular Momentum* (Wiley, New York, 1957).
[41]R. N. Zare, A. L. Schmeltekopf, W. J. Harop, and D. L. Albritton, J. Mol. Spectrosc. 46, 37 (1973).
[42]G. Herzberg, *Spectra of Diatomic Molecules,* 2nd ed. (Van Nostrand, Princeton, N. J., 1950).
[43]F. H. Mies, Phys. Rev. A 7, 942 (1973).
[44]T. H. Dunning and P. J. Hay, J. Chem. Phys. 66, 3767 (1977).
[45]W. J. Stevens and F. Billingsley, Phys. Rev. A 8, 2236 (1973).
[46]R. A. Gordon, J. Chem. Phys. 51, 14 (1969).
[47]F. H. Mies, Phys. Rev. A 7, 957 (1973).
[48]P. S. Julienne and F. H. Mies, J. Phys. B 14, 4335 (1981).